

# Unraveling the Unusual Chemistry of the Hydrogen-Peroxide-Driven Hypergolic Ignition of a Cyanoborohydride Ionic Liquid as a Next-Generation Green Space Propellant

Souvick Biswas,<sup>†</sup> Kazuumi Fujioka,<sup>†</sup> Dababrata Paul, Mason Mcanally, Grace L. Rizzo, Steven D. Chambreau, Stefan Schneider, Rui Sun,<sup>\*</sup> and Ralf I. Kaiser<sup>\*</sup>



Cite This: *J. Phys. Chem. Lett.* 2025, 16, 1831–1839



Read Online

ACCESS |



Metrics & More

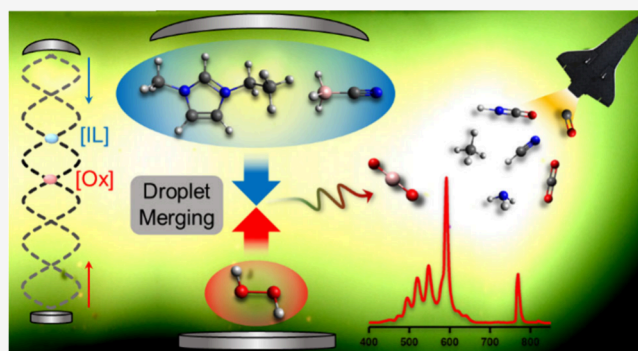


Article Recommendations



Supporting Information

**ABSTRACT:** Hypergolic ionic liquids (HILs) have emerged as promising self-igniting green space propellants in combination with an oxidizer, replacing toxic hydrazine family rocket fuels. Despite numerous new HILs being reported in the literature, there is no systematic study addressing the key reaction mechanism of such hypergolic ignition. Here, the first comprehensive molecular level understanding of this ignition reaction is revealed, exploring a 1-ethyl-3-methylimidazolium cyanoborohydride–hydrogen peroxide ([EMIM][CBH]–H<sub>2</sub>O<sub>2</sub>) green bipropellant pair by a novel chirped-pulse droplet-merging technique in a controlled environment. Mechanistically, the anion [CBH]<sup>−</sup> triggers the hypergolic ignition through facile exoergic oxidation of the boron center yielding boron dioxide (BO<sub>2</sub>) in a barrierless termolecular reaction with two molecules of H<sub>2</sub>O<sub>2</sub>, followed by an enhanced reactivity of the cation [EMIM]<sup>+</sup>, as evidenced from the excess yield of carbon dioxide (CO<sub>2</sub>) and evaluated decay rate constants of [EMIM]<sup>+</sup> *in situ* during the droplet-merging reaction.



Since the elucidation of the mathematical concept of rocket propulsion by Robert H. Goddard in the early 20th century, scientists have pursued the goal of operating faster rockets and reaching distant regions of space beyond the boundary of Earth.<sup>1</sup> After decades of research, hypergolic or self-igniting bipropellants have become a popular choice for distant space missions, circumventing the limitations and complexities of cryogenic propulsion systems.<sup>2</sup> A traditional hypergolic propellant consists of a fuel, which ignites spontaneously (without any ignition source) upon contact with an oxidizer, followed by generating superior thrust and excellent combustion performance. Unfortunately, common hypergolic fuels, for example, hydrazine (N<sub>2</sub>H<sub>4</sub>) and its derivatives, such as methylhydrazine [H<sub>2</sub>NNH-(CH<sub>3</sub>)] and unsymmetric dimethyl hydrazine [UDMH, (CH<sub>3</sub>)<sub>2</sub>N<sub>2</sub>H<sub>2</sub>], used in combination with an oxidizer, like white fuming nitric acid (WFNA, HNO<sub>3</sub>) or dinitrogen tetroxide (N<sub>2</sub>O<sub>4</sub>), are highly toxic, volatile, and carcinogenic.<sup>3,4</sup>

In a major scientific breakthrough by Schneider et al. in 2008, specific “ionic liquids”, salts that are liquid at room temperature, were demonstrated to be hypergolic by testing synthesized 1-allyl-3-methylimidazolium dicyanamide with WFNA as an oxidizer.<sup>5</sup> This introduction to hypergolic ionic liquids (HILs) has revolutionized the development of green bipropellants as potent replacements for the harmful hydrazine family of fuels. Numerous HILs have been synthesized, composed of distinct classes of anions and cations, to enhance reactivity and

performance.<sup>6–28</sup> In general, the anions are shown to initiate and promote the hypergolic ignition.<sup>29</sup> Thus, key electron and fuel-rich anions {e.g., dicyanamide [N(CN)<sub>2</sub>]<sup>−</sup>, nitrocyanoamide [N(NO<sub>2</sub>)(CN)]<sup>−</sup>, borohydride [BH<sub>4</sub>]<sup>−</sup>, and cyanoborate [BH<sub>n</sub>(CN)<sub>4−n</sub>]<sup>−</sup> (*n* = 1–3)}, which can be easily oxidized, have been synthesized, with the high-energy-density boron-centered anions exhibiting superior ignition performance.<sup>30</sup>

Here, we explore the hypergolicity of such an energetic ionic liquid: 1-ethyl-3-methylimidazolium cyanoborohydride ([EMIM][CBH]) with concentrated hydrogen peroxide (H<sub>2</sub>O<sub>2</sub>, ≥80%, w/v) (Figure 1). The constituent ions of the ionic liquid (IL) are purposefully selected. First, cyanoborohydride ([BH<sub>3</sub>(CN)]<sup>−</sup>)-based ILs have exceptional thermal stabilities, moisture insensitivity, and high energy content when compared to energy-rich borohydrides.<sup>14</sup> Second, imidazolium-based ILs possess greater stability than their triazolium or tetrazolium analogues and are suitable for flexible design and synthesis. In particular, [EMIM]<sup>+</sup> in the dicyanamide

**Received:** December 18, 2024

**Revised:** February 6, 2025

**Accepted:** February 11, 2025

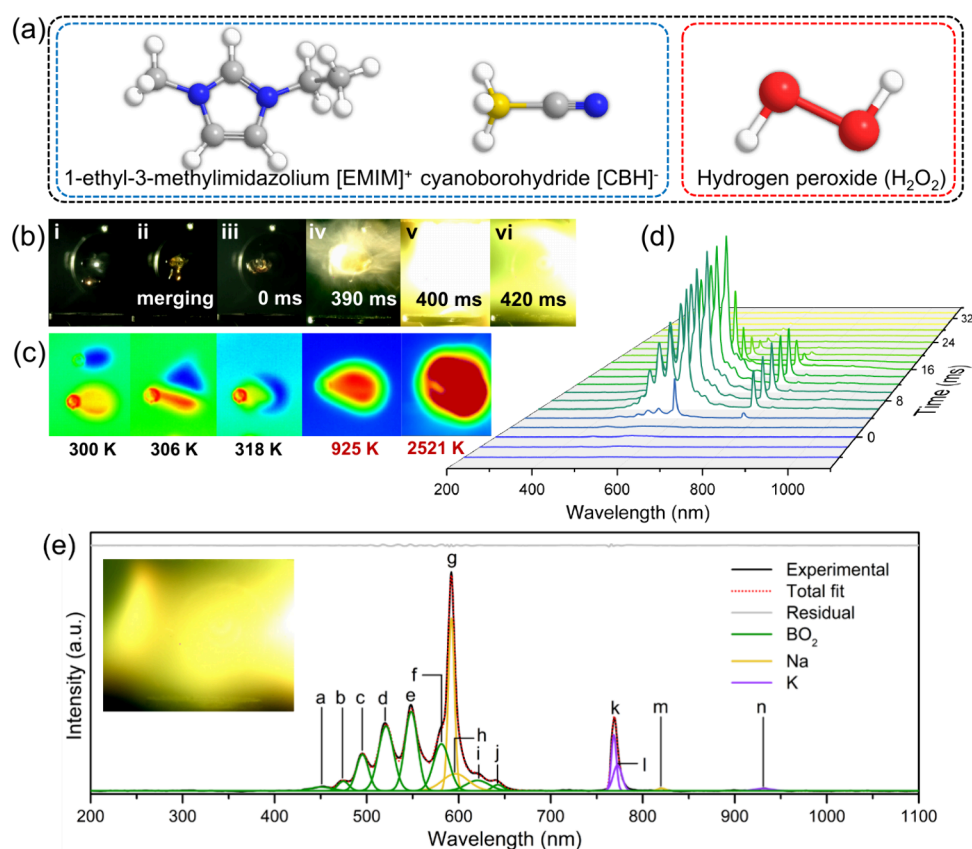


**Figure 1.** (a) Hypergolic bipropellant 1-ethyl-3-methylimidazolium cyanoborohydride ([EMIM][CBH]) and concentrated  $\text{H}_2\text{O}_2$  ( $\geq 80\%$ , w/v). Synchronized, temporally resolved (b) optical and (c) infrared camera images of the droplet-merging event followed by ignition between [EMIM][CBH] and 92% (w/v)  $\text{H}_2\text{O}_2$ . The evolution of the ignition is spectroscopically probed by recording (d) time-resolved emission (UV–vis) spectra. (e) Deconvolution of the most intense flame emission spectrum with the corresponding optical image depicted in the inset.

(DCA) series of ILs has been shown to be most reactive among the imidazolium cations with saturated alkyl substitutions.<sup>31</sup> Overall, [EMIM][CBH] possesses a high thermal stability and has an extremely low vapor pressure (in comparison to hydrazine family fuels), a preferable density ( $0.98 \text{ g cm}^{-3}$ ), and a low viscosity ( $19 \text{ mPa s}$ ).<sup>14,30</sup> Low viscosities are essential for the contact and mixing of reactants, which make it a viable fuel for convenient engine operations. Environmentally unfriendly oxidizers, such as white/red fuming nitric acid ( $\text{HNO}_3$ ) or dinitrogen tetroxide ( $\text{N}_2\text{O}_4$ ), are replaced with a “clean” and ecofriendly alternative, hydrogen peroxide ( $\text{H}_2\text{O}_2$ ),<sup>32–35</sup> making the reactant pair ([EMIM][CBH]– $\text{H}_2\text{O}_2$ ) substantially much “greener” compared to common hypergols.

Here, we report the first comprehensive combined experimental and computational study to unravel the hypergolic ignition chemistry exploiting the [EMIM][CBH]– $\text{H}_2\text{O}_2$  bipropellant pair. It is worth mentioning that the liquid fuel (ionic liquid) and the oxidizer initially interact at the droplet level inside the combustion chamber of the rocket,<sup>36,37</sup> unlike the usual drop tests performed, which have significant surface contribution and excess oxidizer content, thus, do not reflect true ignition delay values and vary largely within different experimental groups. Therefore, the present experiments are performed systematically under controlled conditions in a closed process chamber filled with argon, exploiting a novel droplet-merging method, where quantifiable individually levitated droplets of the HIL and the oxidizer are merged via frequency chirped amplitude modulation of the carrier wave in

an ultrasonic levitator apparatus<sup>38,39</sup> (section S1 of the Supporting Information). Multiple synchronized spectroscopic tools have been utilized in conjunction for the sensitive detection of the gaseous products [Fourier transform infrared (FTIR) spectroscopy] and reaction intermediates [time-resolved ultraviolet–visible (UV–vis) emission and Raman spectroscopy],<sup>40–44</sup> revealing boron dioxide ( $\text{BO}_2$ ) to be the key emitting intermediate driving the hypergolic ignition, as evident from a bright green flame. To unravel the specific roles of the anion and cation during the oxidation, the reaction has been slowed down by diluting the oxidizer ( $\text{H}_2\text{O}_2$ ), thus enabling the identification of the initial reaction intermediates formed *in situ* (Raman spectroscopy). Extensive state-of-the-art electronic structure theory calculations (section S2 of the Supporting Information) complementing the experiments identify the origin of hypergolicity at the molecular level along with the reaction mechanism for the formation of stable products and intermediates.

**Hypergolic Ignition via Chirped-Pulse-Triggered Droplet Merging.** The merging process of the droplets of [EMIM][CBH] and 92%  $\text{H}_2\text{O}_2$  loaded in the lower and upper pressure nodes, respectively, in the standing wave generated in the acoustic levitator, followed by the ignition event, was monitored by high-speed, temporally resolved, synchronized optical and infrared cameras (Figure 1 and Movies S1 and S2 of the Supporting Information). A series of snapshots depict distinct stages comprising (i) levitating reactant droplets (pre-merging), (ii) merging motion upon application of the frequency chirp pulse, and (iii) merging instance accompanied by temperature rise

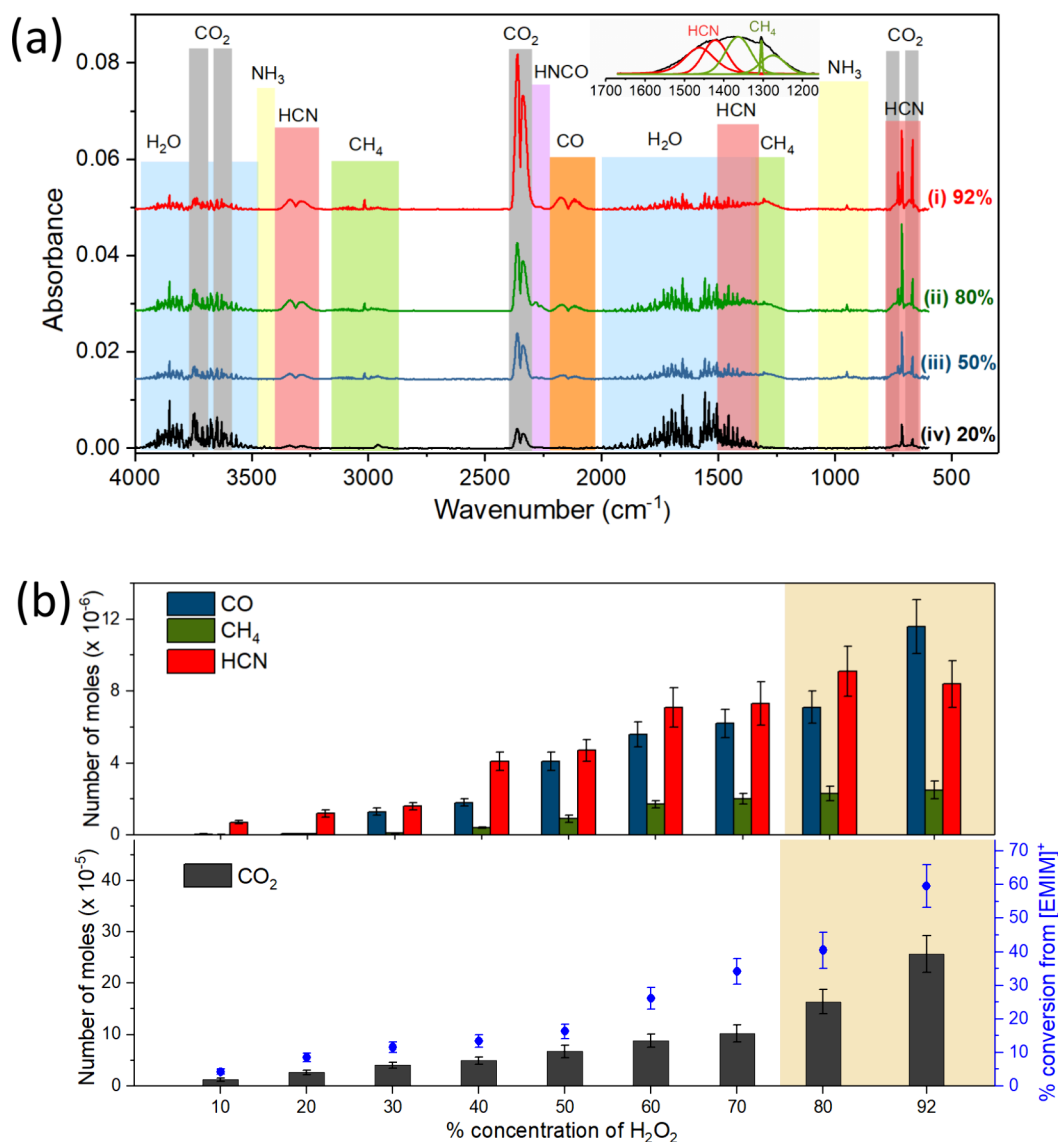


**Figure 2.** (a) FTIR spectra of the gas phase products formed during the reaction of ionic liquid [EMIM][CBH] and selected concentrations of hydrogen peroxide ( $\text{H}_2\text{O}_2$ ) with colored segments for the detected species. Water features are subtracted from the  $1600\text{--}1200\text{ cm}^{-1}$  segment to reveal bands of methane ( $\text{CH}_4$ ) and hydrogen cyanide (HCN). (b) Quantification of the major gaseous products during the reaction of ionic liquid [EMIM][CBH] and distinct concentrations of  $\text{H}_2\text{O}_2$ . The shaded area represents hypergolic reactions. The lower panel shows the percentage conversion of carbon dioxide ( $\text{CO}_2$ ) from the  $[\text{EMIM}]^+$  ion.

(exoergic) with subsequent (iv) initiation and (v and vi) progress of the ignition (combustion) events revealing bright greenish flames with yellowish tints (Figure 1).

Dense smoke formation is associated with the initiation of the ignition (iv), and the temperature exceeds  $2500\text{ K}$  upon expansion of the flame (section S3 of the Supporting Information). An ignition delay (ID) of  $390 \pm 10\text{ ms}$  is determined from the time difference between the merging and initiation of the ignition. Further, testing the IL ([EMIM][CBH]) with diluted  $\text{H}_2\text{O}_2$  (10–80%) revealed the threshold oxidizer concentration for the hypergolicity of this bipropellant pair to be 80% (Figure S6 and Movies S3 and S4 of the Supporting Information). Consequently, the noted ignition delay (ID) is lengthened to  $520 \pm 10\text{ ms}$  compared to that involving 92%  $\text{H}_2\text{O}_2$ , suggesting a direct concentration dependence of the oxidizer. The molar concentration of  $\text{H}_2\text{O}_2$  is required to be about four times with respect to the IL for the occurrence of these hypergolic reactions, as evaluated from the

quantification of the reactant droplets (Table S1 of the Supporting Information).

**Flame Emission Spectra.** The ignition chemistry was probed spectroscopically exploiting UV–vis emission spectroscopy in the  $200\text{--}1100\text{ nm}$  spectral range; the time-resolved emission spectra are displayed in Figure 1d. The temporal evolution of emission spectral intensities indicates the commencement of the ignition, the spread of the flame to its peak intensity, i.e., the combustion of the ionic liquid droplet, followed by no emission, implying the completion of the oxidation process. This time sequence as perceived spectroscopically also mirrors the recordings of the optical camera (Figure 1b). The deconvolution of the emission traces (Figure 1e and Table S2 and Figure S7 of the Supporting Information) reveals dominant emission features of the boron dioxide ( $\text{BO}_2$ ) radical ( $548.4\text{ nm}$ ;  $A\ ^2\Pi_u\text{--}X\ ^2\Pi_g$ ).<sup>45,46</sup> The strong presence of  $\text{BO}_2$  is attributed to the facile oxidation of the  $\text{sp}^3$ -hybridized B center of the [CBH] anion. However, another probable emitting intermediate, boron

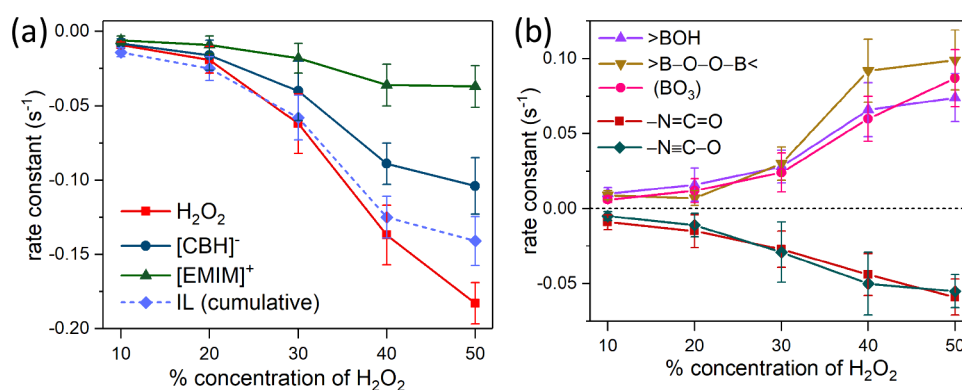


**Figure 3.** Rate constants of the (a) reactants and (b) products/intermediates with respect to the percentage concentration of  $\text{H}_2\text{O}_2$  evaluated by the kinetic fitting of the decay or formation of the characteristic peaks over time as extracted from the consecutive Raman spectra (Figure S15–S26 of the Supporting Information).

monoxide (BO),<sup>47</sup> could not be detected in the emission spectra owing to the intense emissions from boron dioxide. Traces of alkali metals present in the IL are also detectable via their characteristic atomic emission lines of sodium (Na) [589 nm,  $2p^63p^2P \rightarrow 2p^63s^2S$ ; 819 nm,  $2p^63d^2D \rightarrow 2p^63p^2P$ ] and potassium (K) [769 nm,  $3p^64p^2P \rightarrow 3p^64s^2S$ ].<sup>48</sup> The temporal profile of the reactive intermediate  $\text{BO}_2$  (Figure S8 of the Supporting Information) reveals a more or less asymmetric bell-shaped curve with the peak around 10 ms, and the strong ignition lasted about 20 ms. On the contrary, the ignition with 80%  $\text{H}_2\text{O}_2$  was found to be short-lived (Figure S6 of the Supporting Information), suggesting that the oxidation of the B center of  $[\text{CBH}]^-$  is facilitated by a higher concentration of the oxidizer.

**Gas Phase Products.** Irrespective of the ignition, the  $[\text{EMIM}][\text{CBH}]-\text{H}_2\text{O}_2$  merging process was accompanied by the generation of gaseous products, and those were detected via FTIR spectroscopy (Figure 2 and Figure S9 and Table S3 of the Supporting Information). Because the oxidizer contains water as the medium, the broad features (stretching,  $3950\text{--}3490\text{ cm}^{-1}$ ; bending,  $1910\text{--}1320\text{ cm}^{-1}$ ) of water vapor are obvious in the FTIR spectra. The primary combustion product, carbon dioxide ( $\text{CO}_2$ ), is detected from its strong asymmetric stretching ( $2350\text{ cm}^{-1}$ ) and bending ( $667\text{ cm}^{-1}$ ) vibrations along with carbon monoxide (CO) by its stretch at  $2143\text{ cm}^{-1}$ . Characteristic features for hydrogen cyanide (HCN,  $3311$  and  $712\text{ cm}^{-1}$ ), isocyanic acid (HNCO,  $2269\text{ cm}^{-1}$ ), methane ( $\text{CH}_4$ ,  $3150\text{--}2870\text{ cm}^{-1}$ ), and ammonia ( $\text{NH}_3$ ,  $950\text{ cm}^{-1}$ ) are identified. HCN and HNCO plausibly originate upon the decomposition and oxidation of the  $-\text{C}\equiv\text{N}$  functional group existing in  $[\text{CBH}]^-$ . The strong presence of  $\text{CO}_2$  in the spectra suggests the involvement of the carbon-rich cation. In the analogous non-hypergolic reaction of the same IL with WFNA, no  $\text{CO}_2$  was formed, thus assuring a significant reactivity of cation toward  $\text{H}_2\text{O}_2$ .<sup>39</sup> Note that the quantification of the major gaseous products (Figure 2b) from the calibration curves (Figures S10–S13 of the Supporting Information) shows that their amounts ( $\text{CO}_2$ , CO, HCN, and  $\text{CH}_4$ ) increase with the rise in the oxidizer concentration as a general trend, indicating greater decomposition of the IL. The yield of the predominant product,  $\text{CO}_2$ , reaches the maximum conversion efficiency for the hypergolic reaction with 92%  $\text{H}_2\text{O}_2$  of 59% from  $[\text{EMIM}]^+$ , assuming that the latter is its primary source because of the six constituent carbon atoms (Table S4 of the Supporting Information). A slight decrease in the quantity of HCN is observed while increasing the

$\text{H}_2\text{O}_2$  concentration from 80 to 92%, which can be linked to the subsequent oxidation of HCN.<sup>49</sup>

**Reaction Kinetics from Raman Spectroscopy.** The stepwise chemical changes for determining the underlying reaction mechanism have been investigated *in situ* Raman spectroscopically by slowing the reaction using diluted  $\text{H}_2\text{O}_2$  (10–50%). These merging processes are accompanied by a gradual temperature increase with time and gas release via bubble formation in the droplet (Figure S15 of the Supporting Information). The Raman spectra (Figures S14–S16 of the Supporting Information) of the merged droplet reveal several new features (Table S6 of the Supporting Information) of oxygenated intermediates compared to the reactants upon thorough spectral deconvolution, such as cyanato ( $\text{N}\equiv\text{C}-\text{O}$ ), isocyanato ( $\text{N}=\text{C}=\text{O}$ ), boron hydroxy ( $\text{B}-\text{OH}$ ), orthoborate ( $\text{BO}_3$ ), and  $\text{B}(\text{O}-\text{O})\text{B}$  linkage.

The reactivities of the IL and oxidizer have been quantified through the derivation of the decay rate constants as extracted by individual first-order fitting of the time-dependent characteristic Raman peak areas (normalized) during the reaction occurring in the merged droplet (Figures S17 and S23–S26 of the Supporting Information). Similarly, the temporal evolution and the rate constants of formation/decay of the intermediates are also determined (Figures S18 and S23–S26 of the Supporting Information). From the summarized rate constants as a function of the  $\text{H}_2\text{O}_2$  concentration (Figure 3), it is apparent that  $\text{H}_2\text{O}_2$  decays faster than both the anion and cation at a given concentration, and the decay is significantly accelerated upon increasing its concentration.

On the other hand,  $[\text{CBH}]^-$  is found to be consistently more reactive ( $0.104 \pm 0.019\text{ s}^{-1}$ ) in comparison to  $[\text{EMIM}]^+$  ( $0.037 \pm 0.014\text{ s}^{-1}$ ) and measured to be about three times faster at the oxidizer concentration of 50%. The cumulative decay rate constants for the IL (sum of respective rate constants of the anion and cation) follow a trend similar to the decay rates of  $\text{H}_2\text{O}_2$ , but the latter increases rapidly when the oxidizer concentration exceeds 40%. A relevant comparison of similar reactions of this IL with 30%  $\text{H}_2\text{O}_2$  and  $\text{HNO}_3$ , individually, reveals that the decay rate constant of  $[\text{EMIM}]^+$  relative to  $[\text{CBH}]^-$  is much faster in the former ( $0.018 \pm 0.01\text{ s}^{-1}$  versus  $0.04 \pm 0.02\text{ s}^{-1}$ ) than the latter ( $0.007 \pm 0.003\text{ s}^{-1}$  versus  $0.1 \pm 0.01\text{ s}^{-1}$ ).<sup>38</sup> This observed phenomenon ensures the exclusive reactivity of the cation to the present oxidizer ( $\text{H}_2\text{O}_2$ ) quantitatively.

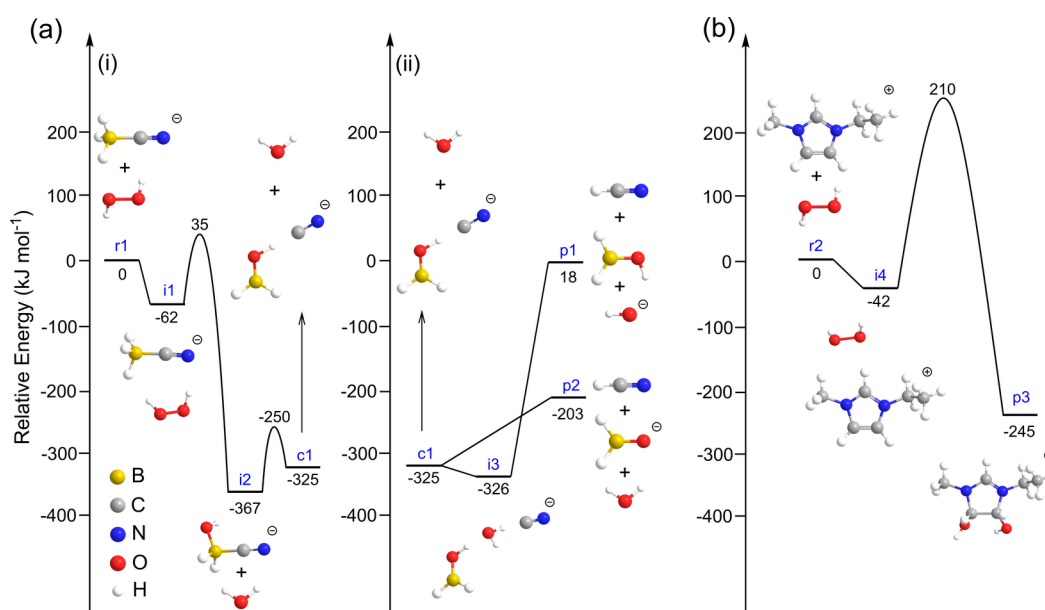


**Figure 4.** PES for the bimolecular reactions of (a)  $[\text{CBH}]^-$  and (b)  $[\text{EMIM}]^+$  with  $\text{H}_2\text{O}_2$ , respectively.

The appearance of the spectral features corresponding to the intermediates at the merging instance suggests that they are formed immediately. From the temporal profiles of these intermediates (Figures S18 and S23–S26 of the Supporting Information), it is evident that the boron-containing species continue forming with the progress of the reaction, whereas intermediates bearing cyanato ( $\text{N}\equiv\text{C}-\text{O}$ ) and isocyanato ( $\text{N}=\text{C}=\text{O}$ ) groups undergo decay for the same. The formation/decay rates for all functional groups have been found to be strongly dependent upon the  $\text{H}_2\text{O}_2$  concentration (Figure 3b), and at a higher oxidizer concentration ( $\geq 40\%$ ), the magnitude of the formation rate constants for boron-containing intermediates exceeds the decay constants of cyanato ( $\text{N}\equiv\text{C}-\text{O}$ ) and isocyanato ( $\text{N}=\text{C}=\text{O}$ ) group-bearing intermediates.

**Electronic Structure Calculation.** To explore the reaction mechanism of the hypergolic  $[\text{EMIM}][\text{CBH}]-\text{H}_2\text{O}_2$  system, the experimental results were merged with extensive electronic structure calculations performed at the B2PLYP/cc-pVTZ//B3LYP/6-31G\* level of theory for determining the zero-point energies of reactants, intermediates, transition states, and products (section S2 of the Supporting Information). Note that the computational treatment considers the whole ionic liquid, where the reactive ion (anion/cation) is only shown or discussed in the figures for simplicity, while the non-reacting ion (cation/anion) remains a spectator in the potential energy surfaces. The potential energy surfaces (PES) for the simplest bimolecular reactions between  $[\text{CBH}]^-$  or  $[\text{EMIM}]^+$  with  $\text{H}_2\text{O}_2$  (Figure 4 and Figure S27 of the Supporting Information) reveal that, although the corresponding entrance channels consist of energetically favored van der Waals complexes (i1 and i4), the subsequent steps of the hydroxyl (OH) reaction with the respective reactants (i1  $\rightarrow$  i2 and i4  $\rightarrow$  p3) possess a significant barrier. The magnitude of the barrier with respect to the separated reactants is significantly higher for the cation (210  $\text{kJ mol}^{-1}$ ) compared to that for the anion (35  $\text{kJ mol}^{-1}$ ); this finding is consistent with the experimentally observed greater reactivity of  $[\text{CBH}]^-$  than  $[\text{EMIM}]^+$  (Figure 3). Upon B–C bond cleavage of  $\text{HOBH}_2\text{CN}^-$  (i2  $\rightarrow$  c1), a H-bonded complex of hydroxyborane ( $\text{H}_2\text{BOH}$ ) and  $\text{CN}^-$  is formed. Consequently, HCN can be formed easily either by proton transfer from

hydroxyborane ( $\text{H}_2\text{BOH}$ ) (c1  $\rightarrow$  p2) or through stepwise complexation (c1  $\rightarrow$  i3) and proton transfer from water (i3  $\rightarrow$  p1) to  $\text{CN}^-$ , while the former path (c1  $\rightarrow$  p2) is exoergic by 203  $\text{kJ mol}^{-1}$  and preferred in comparison to the other path.

However, PES (Figure 5a) depicting the oxidation of  $[\text{CBH}]^-$  by two molecules of  $\text{H}_2\text{O}_2$  forming boron dioxide ( $\text{BO}_2$ ) is found to be entirely submerged in comparison to the separated reactants. The initial van der Waals complex (i5,  $-131 \text{ kJ mol}^{-1}$ ) undergoes a concerted OH reaction substituting the H atom at the B center generating a H-bonded intermediate (i6) traversing the global maximum in the PES ( $-33 \text{ kJ mol}^{-1}$ ). Intermediate i6 eventually releases a hydrated hydroxyl anion ( $\text{H}_2\text{O}\cdots\text{OH}^-$ ) via subsequent hydride elimination from the B center to form a bound complex [i7,  $\text{HB}(\text{OH})\text{CN}\cdots\text{H}_2\text{O}$ ].

Through stepwise B–C bond cleavage (i7  $\rightarrow$  i8), recombination (i8  $\rightarrow$  i9), and isomerization (i9  $\rightarrow$  i10), a new B–N bond is formed [i10,  $(\text{HO})_2\text{BNHCH}$ ], which is ruptured in the next step to produce metaboric acid ( $\text{HOBO}$ ) and methanimine ( $\text{H}_2\text{C}=\text{NH}$ ) (i11). Species in complex i11 are stabilized via the formation of a H-bonded complex, i12. Upon an intermolecular H atom transfer in complex i12, complex i13 ( $\text{CH}_3\text{NH}\cdots\text{BO}_2$ ) is formed, which finally generates doublet radicals: boron dioxide ( $\text{BO}_2$ ) and methylamino ( $\text{CH}_3\text{NH}$ ) (p4). Alternatively, complex i12 can also produce  $\text{BO}_2$  and the aminomethyl radical ( $\text{CH}_2\text{NH}_2$ ) via the decomposition of the newly formed O–C linkage in  $\text{OBOCH}_2\text{NH}_2$  (i14  $\rightarrow$  p5). Ammonia ( $\text{NH}_3$ ), an experimentally detected gas phase reaction product, can be liberated from complex i12 as well via B–C bond formation along i12  $\rightarrow$  i15, followed by a concerted C–N bond cleavage and H atom transfer, forming a van der Waals complex of  $\text{NH}_3$  and a cyclic heteroatomic species ( $\text{HO}-\text{BCO}$ ) (i16), which is then cleaved to the final products. This PES noticeably outlines the facile oxidation mechanism of the B center, ultimately leading to the formation of  $\text{BO}_2$ , which is a predominant emitting intermediate as revealed experimentally and drives the ignition reaction. Evidently, all of the product formation (r3  $\rightarrow$  p4, p5, and p6) channels are exoergic by more than 200  $\text{kJ mol}^{-1}$ , and the released energy can activate subsequent decomposition/oxidation steps, yielding smaller end products.

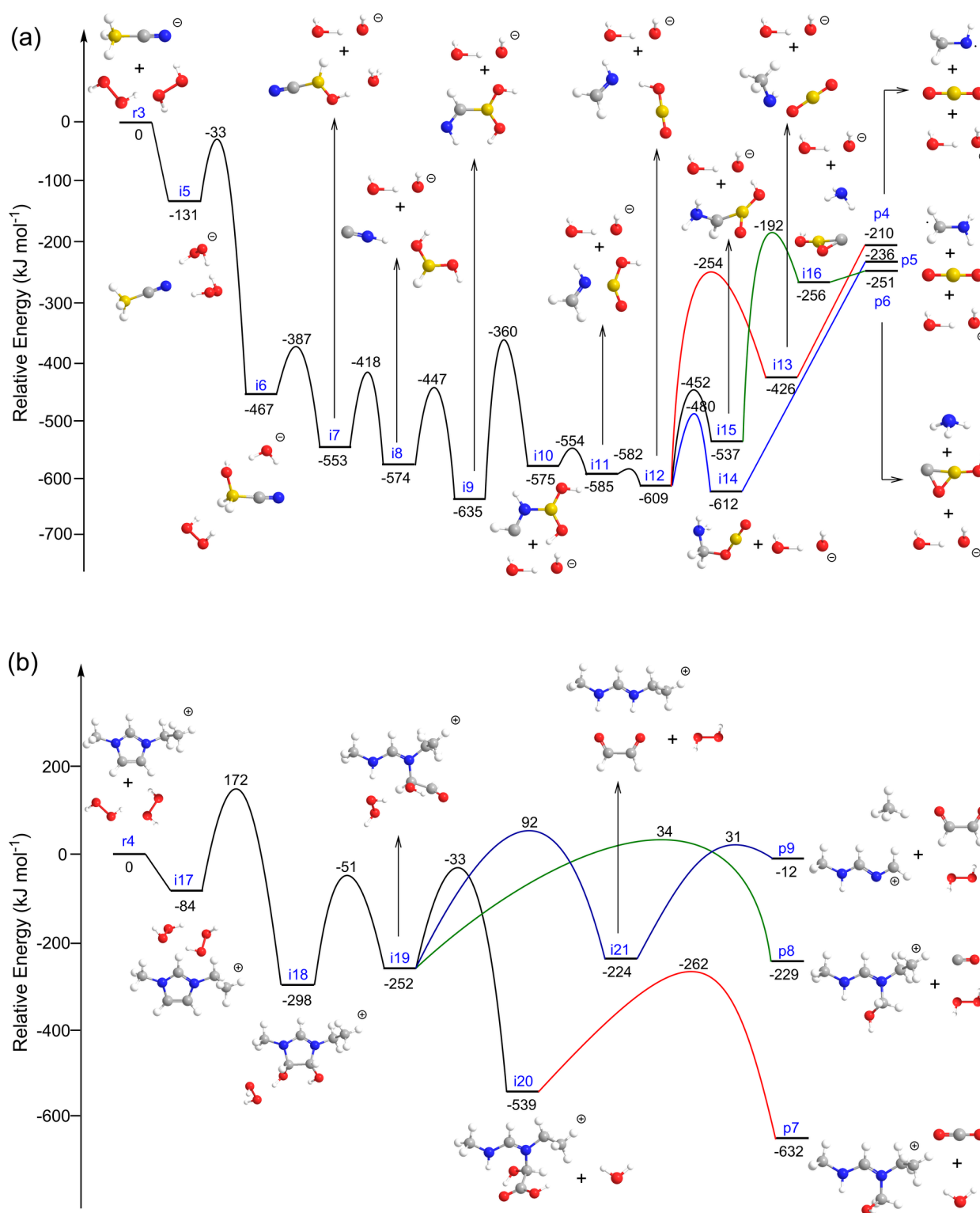


**Figure 5.** PES for the termolecular reactions of (a)  $[\text{CBH}]^-$  and (b)  $[\text{EMIM}]^+$  with two molecules of  $\text{H}_2\text{O}_2$ , respectively.

Similarly, exploring the oxidation of the C center of  $[\text{CBH}]^-$ , several pathways exist, which form major gas phase products, such as  $\text{CO}_2$ ,  $\text{CO}$ ,  $\text{HNCO}$ , and functional groups of the intermediates, as detected by Raman spectroscopy; e.g.,  $^-\text{O}-\text{C}\equiv\text{N}$  and  $-\text{N}=\text{C}=\text{O}$  are determined (Figure S28 of the Supporting Information). These reaction channels are energetically favored, and the energy maximum for the PES is only 4  $\text{kJ mol}^{-1}$ . However, excess  $\text{CO}_2$  as quantified from infrared

spectroscopy explicitly suggests that oxidation of the cation must have a major contribution. Hence, a termolecular reaction of  $[\text{EMIM}]^+$  with two molecules of  $\text{H}_2\text{O}_2$  has also been explored (Figure 5b). The entrance channel leads to the formation of a bound van der Waals complex (i17,  $-84 \text{ kJ mol}^{-1}$ ), followed by a concerted peroxo ( $-\text{O}-\text{O}-$ ) linkage cleavage of  $\text{H}_2\text{O}_2$  and double OH insertion in the adjacent carbon atoms of the imidazolium ring along  $\text{i17} \rightarrow \text{i18}$ . This step is the energy

maximum ( $172 \text{ kJ mol}^{-1}$ ) of the PES and lowered by  $38 \text{ kJ mol}^{-1}$  compared to that of the  $[\text{EMIM}]^+ - \text{H}_2\text{O}_2$  bimolecular reaction. Ring opening (**i18**  $\rightarrow$  **i19**) takes place via C–N bond cleavage in the methyl-substituted side, followed by oxidation to a carboxylic acid terminal group (**i20**). Decarboxylation from complex **i20** yields  $\text{CO}_2$  by accessing an energy barrier of  $277 \text{ kJ mol}^{-1}$  (**i20**  $\rightarrow$  **p7**).  $\text{CO}$  formation from complex **i19** can occur via an energy barrier of  $286 \text{ kJ mol}^{-1}$  (**i19**  $\rightarrow$  **p8**). The oxygenated two-carbon chain becomes detached through a subsequent C–N cleavage along the **i19**  $\rightarrow$  **i21** path, forming glyoxal ( $\text{CHO}-\text{CHO}$ ) and an (*E*)-*N*-((methylamino)methylene)ethaniminium cation, where the latter undergoes a C–C cleavage on the ethyl chain to produce  $\text{CH}_4$  (**p9**). Among all of the exoergic products ( $\text{CH}_4$ ,  $\text{CO}$ , and  $\text{CO}_2$ ) in the PES, the  $\text{CO}_2$  formation path emerges to be most favored and depicts the global minimum ( $-632 \text{ kJ mol}^{-1}$ ) as well. Finally, the extensive oxidation of the residual ethaniminium-containing cation during the exothermic reaction is likely to produce  $\text{CO}$  and  $\text{CO}_2$  as stable end products.

It can be easily noted that the reaction of the  $[\text{CBH}]^- - 2\text{H}_2\text{O}_2$  system involves a submerged barrier and is energetically favored, unlike the analogous reaction of  $[\text{EMIM}]^+$ . This spontaneous reaction sequence consisting of multiple exoergic product formation channels for the oxidation of the anion, in turn, results in the evolution of initial exoergic mixing enthalpy due to droplet merging (Table S9 of the Supporting Information) ranging up to  $11 \text{ kJ mol}^{-1}$ . On the other hand, the high global maximum ( $172 \text{ kJ mol}^{-1}$ ) in the PES of the  $[\text{EMIM}]^+ - 2\text{H}_2\text{O}_2$  system is deemed to be unsurmountable. Alternatively, the high-energy transition state (**i17**  $\rightarrow$  **i18**) can be attained easily from the exoergic product formation steps ranging from  $139$  to  $615 \text{ kJ mol}^{-1}$  (Figure S5a and Figure S28 of the Supporting Information) in the termolecular reactions of the  $[\text{CBH}]^- - 2\text{H}_2\text{O}_2$  system. The above-mentioned finding from an energetic viewpoint is also manifested in the sluggish rate constants (Figure 3) for the decay of  $[\text{EMIM}]^+$  ( $0.037 \pm 0.014 \text{ s}^{-1}$ ) than that of the anion ( $0.104 \pm 0.019 \text{ s}^{-1}$ ) while reacting with  $\text{H}_2\text{O}_2$  (rates mentioned in the case of 50%), as determined from the Raman spectroscopy data. At the molecular level, it can be inferred that the  $\text{IL}-\text{H}_2\text{O}_2$  reaction is initialized by  $[\text{CBH}]^-$  via the facile stepwise oxidation of the B center, followed by the participation of the cation through the simultaneous oxidation of adjacent unsaturated C atoms of the imidazolium ring; overall, the elementary reactions of the anion and cation, individually, are not simultaneous but occur in consecutive steps. Considering both termolecular reactions, four molecules of the oxidizer are consumed per IL molecule, which is consistent with the measured molar ratio of the IL to oxidizer for the occurrence of spontaneous hypergolic ignition. In a much more complicated course of reactions (Figure S29 of the Supporting Information), extensive oxidation of  $[\text{CBH}]^-$  leads to the highly exoergic formation of boric acid ( $\text{H}_3\text{BO}_3$ , **i40**), and coupling of two B centers through a peroxo linkage is also found to be feasible ( $\text{HOBHOOBHOH}$ , **p15**). Vibrational features for both of these have been identified from the Raman spectra.

This combined experimental and computational study of the  $[\text{EMIM}][\text{CBH}] - \text{H}_2\text{O}_2$  bipropellant system by a novel chirped-pulse droplet-merging technique in a controlled environment reveals that the hypergolic ignition originated via the facile exoergic oxidation of the boron center in the anion  $[\text{CBH}]^-$  upon a barrierless termolecular reaction with two molecules of  $\text{H}_2\text{O}_2$ , followed by oxidation of adjacent unsaturated carbon atoms of the imidazolium ring and a subsequent C–N bond

cleavage in the cation  $[\text{EMIM}]^+$ . The spontaneous oxidation of boron leading to the formation of  $\text{BO}_2$ , the key emitting reactive intermediate, was unambiguously detected by temporally resolved emission spectroscopy. The yield of excess  $\text{CO}_2$  quantified by FTIR spectroscopy and moderate decay rate constants of  $[\text{EMIM}]^+$  extracted from Raman spectroscopy, even during the reaction with dilute  $\text{H}_2\text{O}_2$ , provides direct experimental evidence for the enhanced reactivity of the cation. However, the oxidizer ( $\text{H}_2\text{O}_2$ ) concentration-dependent decay constants conclude that  $[\text{CBH}]^-$  reacts faster than the cation, which is correlated to the high initial energy barrier for the latter, contrary to the overall submerged potential energy surface for the former in the case of the respective termolecular reactions. Pivotal initial oxidation steps of the IL were probed mechanistically by identifying the Raman vibrational frequencies for functional groups of intermediates, such as cyanato ( $\text{N}\equiv\text{C}-\text{O}$ ), isocyanato ( $\text{N}=\text{C}=\text{O}$ ), B–OH, and  $\text{BO}_3$ , in the merged droplet *in situ*. Overall, this pioneering work represents the first ever systematic and novel experimental investigation to untangle the complex chemistry emanating from the hypergolicity of ILs with  $\text{H}_2\text{O}_2$ . Further studies are aimed at exploring the structure–reactivity effects originating from distinct organic side groups in the cation for energetic cyanoborohydride ILs and finally extending to other energy-rich anion-containing ILs, thus providing a comprehensive framework of reactivities dictating the hypergolicity of ILs at the molecular level, which is necessitated for the advancement of energy-efficient green hypergolic space propellants.

## ■ ASSOCIATED CONTENT

### SI Supporting Information

The Supporting Information is available free of charge at <https://pubs.acs.org/doi/10.1021/acs.jpcllett.4c03624>.

Experimental and computational methods, temporally resolved optical images with simultaneous flame emission spectra for the hypergolic ignition reaction between  $[\text{EMIM}][\text{CBH}]$  and 80%  $\text{H}_2\text{O}_2$ , flame temperature determination, quantification of molar ratios, peak assignments for the deconvoluted flame emission spectra, temporal profiles of the key emitting intermediates, FTIR spectra of the gas phase products and assignments of the bands, calibration curves of the major gaseous products, percentage yield of carbon dioxide ( $\text{CO}_2$ ) from  $[\text{EMIM}]^+$ , deconvolution and assignment of the Raman spectra for the levitating  $\text{H}_2\text{O}_2$  droplets and merged droplet of  $\text{IL}-\text{H}_2\text{O}_2$ , temporal profiles, kinetic fitting, and evaluated rate constants of the reactants and products during merging reactions probed by Raman spectroscopy, transition states for the reactions of  $[\text{CBH}]^-$  and  $[\text{EMIM}]^+$  with  $\text{H}_2\text{O}_2$ , potential energy profile for the  $[\text{CBH}]^- + 2\text{H}_2\text{O}_2$  reaction forming  $\text{CO}_2$ ,  $\text{CO}$ ,  $\text{HNCO}$ , and  $\text{OCN}^-$ , potential energy profile for extensive oxidation of  $[\text{CBH}]^-$  by  $\text{H}_2\text{O}_2$  forming  $\text{H}_3\text{BO}_3$  and peroxo linkage ( $-\text{O}-\text{O}-$ ) in  $\text{HOBHOOBHOH}$ , enthalpy changes during merging, and coordinates of the reactants, intermediates, transition states, and products (PDF)

Optical movie of droplet-merging and ignition events of the IL with 92%  $\text{H}_2\text{O}_2$  (Movie S1) (MP4)

Infrared movie of droplet-merging and ignition events of the IL with 92%  $\text{H}_2\text{O}_2$  (Movie S2) (MP4)

Optical movie of droplet-merging and ignition events of the IL with 80%  $\text{H}_2\text{O}_2$  (Movie S3) (MP4)

Infrared movie of droplet-merging and ignition events of the IL with 80% H<sub>2</sub>O<sub>2</sub> (Movie S4) (MP4)

Optical movie of droplet-merging and ignition events of the IL with 50% H<sub>2</sub>O<sub>2</sub> (Movie S5) (MP4)

Infrared movie of droplet-merging and ignition events of the IL with 50% H<sub>2</sub>O<sub>2</sub> (Movie S6) (MP4)

## AUTHOR INFORMATION

### Corresponding Authors

**Rui Sun** – Department of Chemistry, University of Hawai'i at Manoa, Honolulu, Hawaii 96822, United States;

orcid.org/0000-0003-0638-1353; Email: ruisun@hawaii.edu

**Ralf I. Kaiser** – Department of Chemistry, University of Hawai'i at Manoa, Honolulu, Hawaii 96822, United States;

orcid.org/0000-0002-7233-7206; Email: ralfk@hawaii.edu

### Authors

**Souvick Biswas** – Department of Chemistry, University of Hawai'i at Manoa, Honolulu, Hawaii 96822, United States;

orcid.org/0000-0002-1643-2663

**Kazuumi Fujioka** – Department of Chemistry, University of Hawai'i at Manoa, Honolulu, Hawaii 96822, United States

**Dababrata Paul** – Department of Chemistry, University of Hawai'i at Manoa, Honolulu, Hawaii 96822, United States;

orcid.org/0000-0002-5264-3601

**Mason Mcanally** – Department of Chemistry, University of Hawai'i at Manoa, Honolulu, Hawaii 96822, United States;

orcid.org/0009-0000-7799-9914

**Grace L. Rizzo** – Department of Chemistry, University of Hawai'i at Manoa, Honolulu, Hawaii 96822, United States

**Steven D. Chambreau** – Air Force Research Laboratory, Edwards Air Force Base, California 93524, United States

**Stefan Schneider** – Air Force Research Laboratory, Edwards Air Force Base, California 93524, United States

Complete contact information is available at:

<https://pubs.acs.org/10.1021/acs.jpcllett.4c03624>

### Author Contributions

<sup>†</sup>Souvick Biswas and Kazuumi Fujioka contributed equally to this work. Ralf I. Kaiser designed the experiments. Souvick Biswas, Mason Mcanally, and Grace L. Rizzo carried out the experiments. Souvick Biswas and Dababrata Paul analyzed the data. Steven D. Chambreau and Stefan Schneider carried out the synthesis. Kazuumi Fujioka and Rui Sun performed the theoretical calculations. Souvick Biswas wrote the original draft. Souvick Biswas, Rui Sun, and Ralf I. Kaiser revised the draft. All of the authors discussed the data.

### Notes

The authors declare no competing financial interest.

## ACKNOWLEDGMENTS

This work was supported by the Air Force Office of Scientific Research (AFOSR, FA9550-21-1-0377). The authors appreciate the Information Technology Service (ITS) from the University of Hawaii at Manoa for the computational resources.

## REFERENCES

(1) Lehman, M. *Robert H. Goddard*; Da Capo Press: Boston, MA, 1988.

(2) Sutton, G. P. *History of Liquid Propellant Rocket Engines*; American Institute of Aeronautics and Astronautics (AIAA): Reston, VA, 2006; DOI: 10.2514/4.868870.

(3) Nguyen, H. N.; Chenoweth, J. A.; Beberta, V. S.; Albertson, T. E.; Nowadly, C. D. The Toxicity, Pathophysiology, and Treatment of Acute Hydrazine Propellant Exposure: A Systematic Review. *Mil. Med.* **2021**, *186*, e319–e326.

(4) Liquid Propulsion Committee. *Special Project: Fire, Explosion, Compatibility, and Safety Hazards of Nitrogen Tetroxide (AIAA SP-086-2001)*; American Institute of Aeronautics and Astronautics (AIAA): Reston, VA, 2001; DOI: 10.2514/4.474965.001.

(5) Schneider, S.; Hawkins, T.; Rosander, M.; Vaghjiani, G.; Chambreau, S.; Drake, G. Ionic Liquids as Hypergolic Fuels. *Energy Fuels* **2008**, *22*, 2871–2872.

(6) Gao, H.; Shreeve, J. n. M. Ionic Liquid Solubilized Boranes as Hypergolic Fluids. *J. Mater. Chem.* **2012**, *22*, 11022–11024.

(7) He, L.; Tao, G.-H.; Parrish, D. A.; Shreeve, J. M. Nitrocyamamide-Based Ionic Liquids and Their Potential Applications as Hypergolic Fuels. *Chem. - Eur. J.* **2010**, *16*, 5736–5743.

(8) Lauck, F.; Balkenhohl, J.; Negri, M.; Freudenmann, D.; Schlechtriem, S. Green Bipropellant Development – A Study on The Hypergolicity of Imidazole Thiocyanate Ionic Liquids with Hydrogen Peroxide in an Automated Drop Test Setup. *Combust. Flame* **2021**, *226*, 87–97.

(9) Li, S.; Gao, H.; Shreeve, J. M. Borohydride Ionic Liquids and Borane/Ionic-Liquid Solutions as Hypergolic Fuels with Superior Low Ignition-Delay Times. *Angew. Chem., Int. Ed.* **2014**, *53*, 2969–2972.

(10) Schneider, S.; Hawkins, T.; Ahmed, Y.; Rosander, M.; Hudgens, L.; Mills, J. Green Bipropellants: Hydrogen-Rich Ionic Liquids that Are Hypergolic with Hydrogen Peroxide. *Angew. Chem., Int. Ed.* **2011**, *50*, 5886–5888.

(11) Wang, K.; Zhang, Y.; Chand, D.; Parrish, D. A.; Shreeve, J. M. Boronium-Cation-Based Ionic Liquids as Hypergolic Fluids. *Chem. - Eur. J.* **2012**, *18*, 16931–16937.

(12) Zhang, Q.; Shreeve, J. M. Energetic Ionic Liquids as Explosives and Propellant Fuels: A New Journey of Ionic Liquid Chemistry. *Chem. Rev.* **2014**, *114*, 10527–10574.

(13) Zhang, Q.; Shreeve, J. M. Ionic Liquid Propellants: Future Fuels for Space Propulsion. *Chem. - Eur. J.* **2013**, *19*, 15446–15451.

(14) Zhang, Q.; Yin, P.; Zhang, J.; Shreeve, J. M. Cyanoborohydride-Based Ionic Liquids as Green Aerospace Bipropellant Fuels. *Chem. - Eur. J.* **2014**, *20*, 6909–6914.

(15) Zhang, Y.; Gao, H.; Joo, Y. H.; Shreeve, J. M. Ionic Liquids as Hypergolic Fuels. *Angew. Chem., Int. Ed.* **2011**, *50*, 9554–9662.

(16) Zhang, Y.; Shreeve, J. n. M. Dicyanoborate-Based Ionic Liquids as Hypergolic Fluids. *Angew. Chem., Int. Ed.* **2011**, *50*, 935–937.

(17) Mota, F. A. S.; Fei, L.; Liu, M.; Jiang, J.; Tang, C. Novel Hypergolic Green Fuels with Hydrogen Peroxide for Propulsion Systems. *J. Propul. Power* **2024**, *40*, 207–219.

(18) Mota, F. A. S.; Dias, G. S.; Fei, L.; Tang, C. Ignition Envelope and Bubbly Spray Combustion of a Cost-Effective Self-Igniting Fuel with Rocket-Grade Hydrogen Peroxide. *Combust. Flame* **2024**, *270*, No. 113744.

(19) Wang, B.; Wang, Z.; Jin, Y.; Wang, K. Designing Difunctional Promoters for Hypergolic Ignitions of Green Bipropellants Combining Ionic Liquids with H<sub>2</sub>O<sub>2</sub>. *Ind. Eng. Chem. Res.* **2022**, *61*, 17433–17439.

(20) Li, X.; Huo, H.; Li, H.; Nie, F.; Yin, H.; Chen, F.-X. Cyanotetrazolylborohydride (CTB) Anion-Based Ionic Liquids with Low Viscosity and High Energy Capacity as Ultrafast-Igniting Hypergolic Fuels. *Chem. Commun.* **2017**, *53*, 8300–8303.

(21) Pialat, A.; Kitos, A. A.; Witkowski, T. G.; Cook, C.; Wang, S.; Hu, A.; Murugesu, M. Achieving Short Ignition Delay and High Specific Impulse with Cyanoborohydride-Based Hypergolic Ionic Liquids. *New J. Chem.* **2022**, *46*, 21212–21220.

(22) Li, J.; Weng, X.; Tang, C.; Zhang, Q.; Fan, W.; Huang, Z. The Ignition Process Measurements and Performance Evaluations for Hypergolic Ionic Liquid Fuels: [EMIm][DCA] and [BMIm][DCA]. *Fuel* **2018**, *215*, 612–618.

- (23) Isaac Sam, I.; Gayathri, S.; Santhosh, G.; Cyriac, J.; Reshmi, S. Exploring the Possibilities of Energetic Ionic Liquids as Non-Toxic Hypergolic Bipropellants in Liquid Rocket Engines. *J. Mol. Liq.* **2022**, *350*, No. 118217.
- (24) Mota, F. A. S.; Fei, L.; Tang, C.; Huang, Z.; Costa, F. S. Hypergolic Ignition Behaviors of Green Propellants with Hydrogen Peroxide: The TMEDA/DMEA System. *Fuel* **2023**, *336*, No. 127086.
- (25) Mota, F. A. S.; Liu, M.; Mohsen, A. A. A.; Yao, X.; Mai, Z.; Tang, C. Development of Polyamine/Alkanolamine-Based Hypergolics with Hydrogen Peroxide: A New Route to N-methylimidazole with MDEA as a Promising Green Fuel. *Fuel* **2024**, *357*, No. 129798.
- (26) Dias, G. S.; da Silva Mota, F. A.; Fei, L.; Tang, C.; de Souza Costa, F. Gelled Hydrogen Peroxide: Hypergolic Reaction with Low Toxicity Fuel by Drop and Impinging Jets Tests. *Acta Astronaut.* **2024**, *222*, 471–480.
- (27) Mota, F. A. S.; Dias, G. S.; Machado, D. A.; Andrade, J. C.; Costa, F. S.; Fei, L.; Tang, C. Characterization of the Hypergolic Ignition of Green Fuels with Hydrogen Peroxide by Drop Test and Jet Impingement. *Combust. Flame* **2024**, *267*, No. 113567.
- (28) Wu, Y.; Kong, X.; Ao, Y.; Mota, F. A. S.; Wang, J.; Zhang, Y.; Tang, C.; Huang, Z. Understanding the Synergistic Effect in Green Propellants 2-Azido-N,N-Dimethylethanamine and Tetramethylethylenediamine: From Drop Test to Gas-Phase Autoignition. *Combust. Flame* **2024**, *268*, No. 113590.
- (29) Sun, C.; Tang, S. Hypergolic Ionic Mixtures with Task-Specific Ions: A New Strategy to Improve Performances of Ionic Liquids as Propellant Fuels. *Combust. Flame* **2021**, *228*, 107–113.
- (30) Zhang, Z.; Zhao, Z.; Wang, B.; Zhang, J. Boron Based Hypergolic Ionic Liquids: A Review. *Green Energy Environ.* **2021**, *6*, 794–822.
- (31) Sun, C.; Tang, S.; Zhang, X. Role of Cation Structures for Energetic Performance of Hypergolic Ionic Liquids. *Energy Fuels* **2017**, *31*, 10055–10059.
- (32) Kopacz, W.; Okninski, A.; Kasztankiewicz, A.; Nowakowski, P.; Rarata, G.; Maksimowski, P. Hydrogen Peroxide – A Promising Oxidizer for Rocket Propulsion and Its Application in Solid Rocket Propellants. *FirePhysChem.* **2022**, *2*, 56–66.
- (33) Seo, M.; Bhosale, V. K.; Im, H.; Kwon, S. Performance Improvement of Triglyme-Based Fuels Using an Ionic Liquid With Hydrogen Peroxide. *Combust. Flame* **2024**, *270*, No. 113719.
- (34) Bhosale, V. K.; Jeong, J.; Choi, J.; Churchill, D. G.; Lee, Y.; Kwon, S. Additive-Promoted Hypergolic Ignition of Ionic Liquid with Hydrogen Peroxide. *Combust. Flame* **2020**, *214*, 426–436.
- (35) Bhosale, V. K.; Jeong, J.; Kwon, S. Ignition of Boron-Based Green Hypergolic Fuels with Hydrogen Peroxide. *Fuel* **2019**, *255*, No. 115729.
- (36) Webber, W. T.; Hoffman, R. J. Mechanistic Model for Analysis of Pulse-Mode Engine Operation. *J. Spacecr. Rockets* **1975**, *12*, 113–117.
- (37) Zhang, D.; Yu, D.; Zhang, P.; Yuan, Y.; Yue, L.; Zhang, T.; Fan, X. Hypergolic Ignition Modulated by Head-on Collision, Inter-mixing and Convective Cooling of Binary Droplets with Varying Sizes. *Int. J. Heat Mass Transfer* **2019**, *139*, 475–481.
- (38) Biswas, S.; Antonov, I.; Fujioka, K.; Rizzo, G. L.; Chambreau, S. D.; Schneider, S.; Sun, R.; Kaiser, R. I. Unraveling the Initial Steps of the Ignition Chemistry of The Hypergolic Ionic Liquid 1-Ethyl-3-Methylimidazolium Cyanoborohydride ([EMIM][CBH]) with Nitric Acid (HNO<sub>3</sub>) Exploiting Chirped Pulse Triggered Droplet Merging. *Phys. Chem. Chem. Phys.* **2023**, *25*, 6602–6625.
- (39) Biswas, S.; Fujioka, K.; Antonov, I.; Rizzo, G. L.; Chambreau, S. D.; Schneider, S.; Sun, R.; Kaiser, R. I. Hypergolic Ionic Liquids: To Be or Not to Be? *Chem. Sci.* **2024**, *15*, 1480–1487.
- (40) Paul, D.; Biswas, S.; Yeom, H.; Na, K.; Pantoya, M. L.; Kaiser, R. I. Unraveling the Nanosheet Zeolite-Catalyzed Combustion of Aluminum Nanoparticles-Doped exo-Tetrahydrodicyclopentadiene (JP-10) Energetic Fuel. *ACS Appl. Mater. Interfaces* **2024**, *16*, 53938–53949.
- (41) Rizzo, G. L.; Biswas, S.; Antonov, I.; Miller, K. K.; Pantoya, M. L.; Kaiser, R. I. Exotic Inverse Kinetic Isotopic Effect in the Thermal Decomposition of Levitated Aluminum Iodate Hexahydrate Particles. *J. Phys. Chem. Lett.* **2023**, *14*, 2722–2730.
- (42) Rizzo, G. L.; Biswas, S.; Pantoya, M. L.; Kaiser, R. I. Unraveling the Ignition Chemistry of singly Levitated Aluminum Iodate Hexahydrate (AIH) Particles. *Chem. Phys. Lett.* **2024**, *842*, No. 141212.
- (43) Rizzo, G. L.; Biswas, S.; Ka, D.; Zheng, X.; Kaiser, R. I. Untangling the Efficient Boron-Initialized Hydroxyl-Terminated Polybutadiene Combustion for High Energetic Solid Propulsion Systems. *J. Phys. Chem. A* **2025**, *129*, 288–300.
- (44) Biswas, S.; Paul, D.; Mondal, K.; Kaiser, R. I. Simulating Atmospheric Freezing of Single Aqueous Droplets to Ice in a Cryogenically Cooled Ultrasonic Levitator. *Proc. Natl. Acad. Sci. U.S.A.* **2025**, *122* (6), No. e2425543122.
- (45) Fried, A.; Mathews, C. W. The Resonance Fluorescence of BO<sub>2</sub> Excited by a Pulsed Dye-Laser. *Chem. Phys. Lett.* **1977**, *52*, 363–367.
- (46) Johns, J. W. C. The Absorption Spectrum of BO<sub>2</sub>. *Can. J. Phys.* **1961**, *39*, 1738–1768.
- (47) Baier, M. J.; McDonald, A. J.; Clements, K. A.; Goldenstein, C. S.; Son, S. F. High-Speed Multi-Spectral Imaging of the Hypergolic Ignition of Ammonia Borane. *Proc. Combust. Inst.* **2021**, *38*, 4433–4440.
- (48) Kramida, A.; Ralchenko, Y.; Reader, J.; NIST ASD Team NIST Atomic Spectra Database (Version 5.10); National Institute of Standards and Technology (NIST): Gaithersburg, MD, 2022; DOI: 10.18434/T4W30F (accessed Nov 4, 2023).
- (49) Dagaut, P.; Glarborg, P.; Alzueta, M. U. The Oxidation of Hydrogen Cyanide and Related Chemistry. *Prog. Energy Combust. Sci.* **2008**, *34*, 1–46.